Resonant α scattering of ^{6}He: Limits of clustering in ^{10}Be

D. Suzuki, A. Shore, W. Mittig, J. J. Kolata, D. Bazin, M. Ford, T. Ahn, F. D. Becchetti, S. Beceiro Novo, D. Ben Ali, B. Bucher, J. Browne, X. Fang, M. Febbraro, A. Fritsch, E. Galyaev, A. M. Howard, N. Keeley, W. G. Lynch, M. Ojaruega, A. L. Roberts, and X. D. Tang

Resonant α scattering of ^{6}He: limits of clustering in ^{10}Be

D. Suzuki,[1,2,*] A. Shore,[1,3] W. Mittig,[1,3] J.J. Kolata,[4] D. Bazin,[1] M. Ford,[1,†]

T. Ahn,[1] F.D. Becchetti,[5] D. Ben Ali,[6] B. Bucher,[4] J. Browne,[4,1,3]

X. Fang,[4] M. Febbraro,[5] A. Fritsch,[1,3] E. Galyaev,[1] A.M. Howard,[4]

N. Keeley,[7] W.G. Lynch,[1,3] M. Ojaruega,[5] A.L. Roberts,[4] and X.D. Tang[4]

[1] *National Superconducting Cyclotron Laboratory,*

Michigan State University, East Lansing, Michigan 48824-1321, USA

[2] *Institut de Physique Nucléaire, IN2P3-CNRS,*

Université Paris-Sud, F-91406 Orsay, France

[3] *Department of Physics and Astronomy, Michigan State University,*

East Lansing, Michigan 48824-1321, USA

[4] *Department of Physics, University of Notre Dame,*

Notre Dame, Indiana 46556-5670, USA

[5] *Department of Physics, University of Michigan,*

Ann Arbor, Michigan 48109-1040, USA

[6] *Département de Physique, Université Paris-Sud, F-91403 Orsay, France*

[7] *National Centre for Nuclear Research,*

ul. Andrzeja Sołtana 7, 05-400 Otwock, Poland

(Dated: April 7, 2013)

Abstract

The structure of ^{10}Be was studied via resonant α-particle scattering of a neutron-rich ^{6}He beam. A time projection chamber, PAT-TPC, was operated in an active-target mode to provide a gaseous ^{4}He target and trace the beam and reaction products traversing its active tracking volume. This significantly lowered the detection threshold of reaction products at low energies. Elastic scattering, inelastic scattering to the ^{6}He 2^+ state, and the ^{6}He$(\alpha, 2n)^8$Be reaction were measured below an energy of 6 MeV in the center-of-mass frame. Continuous spectra of excitation functions and angular distributions were obtained from unambiguously-identified recoiling α particles for the elastic and inelastic channels. While a resonance of the 4^+ state at 10.15 MeV in ^{10}Be previously reported was confirmed, no other resonances were identified in the elastic channel over the measured energy region. The results are in line with antisymmetric molecular dynamics calculations that predict the limits of α clustering in high-spin states due to a spin-orbit force.

PACS numbers: 24.30.Gd, 25.55.Ci, 27.20.+n, 29.40.Cs

* e-mail: suzuki@ipno.in2p3.fr

† Present address: Air Force Institute of Technology (AFIT), WPAFB, Ohio 45433, USA

I. INTRODUCTION

Clustering of α particles is a unique aspect of nuclear correlations. It is known that α clustering often occurs in light nuclei along the $N = Z$ line as already suggested since 1930s to explain their level schemes [1–3]. Archetypal examples are the ground state of ^{8}Be and the second 0^+ state of ^{12}C (referred to as "Hoyle" state) [4, 5], manifesting well-developed 2α and 3α clusters, respectively, and likewise further heavier systems such as 4α states in ^{16}O [6] or 6α states in ^{24}Mg [7]. These cluster states, which exclusively consist of α particles, have been providing a unique playground to discuss bosonic condensations [6, 8, 9] or geometries of multiple quantum objects [3, 7] in femtometer-scale systems.

The structure of the nucleus, a quantum many-body system, can drastically change with addition or removal of nucleons. How, if at all, do these nucleons affect α clustering in nuclei? The structure of ^{11}B, the nucleus with one proton removed from ^{12}C, was recently studied via the (d, d') reaction [10]. The large monopole strength extracted for the $3/2^-$ state at 8.56 MeV indicates a well-developed $2\alpha + t$ cluster structure, suggesting that the clustering nature of the Hoyle state in ^{12}C persists in the presence of a proton hole. Theoretical studies on neutron-rich beryllium isotopes that trace the cluster evolution away from ^{8}Be also predict the persistence of 2α clusters in the neutron-excess systems ^{10}Be [11–24] and ^{12}Be [25, 26]. It is further suggested that the unique correlation of neutrons and 2α clusters diversifies the evolution of structure. The formation of predicted structures, such as neutron-molecular orbitals [15, 16, 25, 26] or a di-neutron pair around 2α cores [24], plays an important role to stabilize 2α cores [16, 25, 26], break the axial symmetry [24], or possibly quench the shell gap at the magic number 8 [25–28]. However, there are limited experimental data to support such interplay between α clusters and valence neutrons.

In the present paper, we report on the excitation properties of ^{10}Be via resonant α scattering of ^{6}He. The neutron-rich ^{10}Be nucleus is a simple system consisting of ^{8}Be plus $2n$. Nevertheless, ^{10}Be involves a complex level scheme that features three rotational bands built on the 0^+ ground state, the 1^- state at 5.96 MeV, and the second 0^+ state at 6.18 MeV. Theoretically, the origin of these bands is explained in terms of molecular orbitals of valence neutrons [15, 16] . In this picture, these neutrons are delocalized over the 2α cores and occupy different orbital levels, thus different intrinsic states. There has been a number of studies conducted in search of experimental signatures of the predicted intrinsic structures.

64 Particularly high-spin members of the $0^+_{\text{g.s.}}$ and 0^+_2 bands have been searched using different

65 reaction probes. The 4^+ member of the 0^+_2 band was first speculated for the state at 10.2 MeV

66 found in a study of the ^{7}Li + ^{7}Li reaction [29]. While this state was later confirmed at

67 10.15(2) MeV using the ^{7}Li + ^{6,7}Li reactions, a spin-parity of 3^- was assigned from the

68 angular correlation of α and ^{6}He particles following the α decay [30]. Another angular

69 correlation study using the ^{6}He + ^{6,7}Li reactions, however, gave a conflicting assignment

70 of 4^+, indicating that the method depends on the model assumed in reaction analyzes [31].

71 A spin-parity of 4^+ was assigned without such assumptions in a recent measurement of α

72 scattering from ^{6}He, in which the 10.15-MeV state in ^{10}Be was resonantly populated and

73 the angular distribution was characteristic of the angular momentum 4 [32]. The associated

74 large width for α emission was interpreted as a strong indication of the predicted molecular

75 structure. The 4^+ member of the $0^+_{\text{g.s.}}$ band is considered the 4^+ state at 11.76 MeV [33]. The

76 α clustering of the ground state band is naïvely assumed from its level scheme being nearly

77 equal to ^{8}Be, having the 2^+ state at 3.37 MeV (^{8}Be 2^+_1 3.03 MeV) and the 4^+ state at 11.76

78 MeV (^{8}Be 4^+_1 11.4 MeV) [33]. This assumption has been supported by theoretical studies

79 that describe well the level scheme within the molecular orbital picture [15, 16, 18, 19, 21,

80 22, 24]. The possibility of a shell-model-like structure was, however, recently discussed in a

81 study of ^{10}Be via inelastic scattering with ^{12}C [34], where the excitation to the 4^+ member

82 of the $0^+_{\text{g.s.}}$ band was not observed. This suggests there is a delicate balance between the

83 persistence and the dissociation of α clusters in ^{10}Be, and merits further elucidation.

84 In this study, we measured scattering of ^{6}He on α particles at low energies to resonantly

85 populate states in ^{10}Be. The resonance strength, which is related to the decay width for

86 α emission, is an important indicator of the degree of α clusterization [32, 35]. Elastic α

87 scattering of ^{6}He was measured in a few previous studies [32, 36–38]. The measurement by

88 Ter-Akorpian et $al.$ was performed at a center-of-mass energy ($E_{\text{c.m.}}$) of 60.3 MeV [36], while

89 those of Raabe et $al.$ were at 11.6 and 15.9 MeV [37, 38]. At these higher energies, the

90 data are well reproduced by direct reaction analyses based on the coupled-discretized con-

91 tinuum channels formalism [39] and the coupled-reaction channel formalism [40]. Freer et $al.$

92 recently measured scattering at low energies below 5 MeV, and identified a resonance orig-

93 inating from the 4^+ state at 10.15 MeV [32]. Their measurement was, however, performed

94 at only three center-of-mass energies, namely $E_{\text{c.m.}}$ = 2.44, 3.00 and 4.44 MeV. Therefore,

95 there was no continuous excitation spectrum, which hampers the ability to thoroughly scan

resonances over a given excitation energy region. In addition, the reconstruction of the reaction kinematics had an ambiguity because recoiling α particles and scattered ^{6}He particles were not differentiated, while the obtained angular distribution was correctly analyzed using simulations that took this ambiguity into account. In the present study, we measured continuous excitation functions over a wide energy range of $E_{\mathrm{c.m.}} = 2-6$ MeV and reconstructed angular distributions from unambiguously-identified recoiling α particles. This allowed us to survey resonances over the energy domain where the 4^+ members of the ground-state band and the second 0^+ band are located, as well as the region where some other resonances have been predicted [14, 23].

An experimental challenge is the detection of low-energy helium particles from scattering, which quickly lose their energy in the target medium. We used a time projection chamber (TPC) in the "active-target" mode to address this issue, where the gas of the TPC serves simultaneously as the α-particle target as well as the tracking medium of reaction products. This allows measurements of the energy and scattering angle of particles which stop inside the target. This setup is capable of measuring not only elastic scattering, but also inelastic scattering and neutron-emission channels such as ^{6}He$(\alpha, 2n)^8$Be, in which negative reaction Q values further lower the energy of the reaction products. This new method also enables the determination of reaction energies from the direct measurement of reaction positions. In the thick target method [41], the established and widely-used method to measure continuous excitation functions in inverse kinematics, the reaction energy is indirectly obtained from the energy of recoiling particles assuming a given kinematical scenario. This usually requires several different settings for beam energies to avoid mixing elastic and inelastic scattering. In our method, the unambiguous identification of the reaction energy allows us to differentiate reaction channels, thus enabling us to cover a wide energy range in a single measurement.

II. EXPERIMENT

The experiment was performed at the *TwinSol* radioactive nuclear beam facility [42] at the University of Notre Dame. Scattering of ^{6}He on α particles was measured using the Prototype Active-Target Time-Projection Chamber (PAT-TPC) [43]. A secondary ^{6}He beam with an energy of 15 MeV was produced using the ^{7}Li$(d, {}^3$He$)^6$He reaction. A stable ^{7}Li beam was accelerated to 29.2 MeV by the FN Tandem accelerator and impinged on a

gaseous deuterium target. The pressure of the deuterium gas was 1200 mm-Hg on average. The gas cell had windows consisting of two 4.2-mg/cm^2 Havar foils 2.5 cm apart along the beam axis. The effective path length in the cell was longer by a few millimeters due to bowing of the foils under pressure. Outgoing reaction products were collected and focused by a pair of superconducting solenoidal magnets of the *TwinSol* device [42]. A 6-mg/cm^2 CH$_2$ foil was placed at the cross-over point between the two magnets, which significantly slowed down higher Z contaminants, namely Li, from the primary beam, and greatly improved the purity of the ^{6}He beam. During the beam tuning, a silicon E-ΔE telescope was used in front of the PAT-TPC as a beam monitor. The beam was predominantly composed of ^{6}He and the main contaminant was ^{4}He with an energy of about 22 MeV. The telescope was then removed from the beam line once the beam tuning was completed.
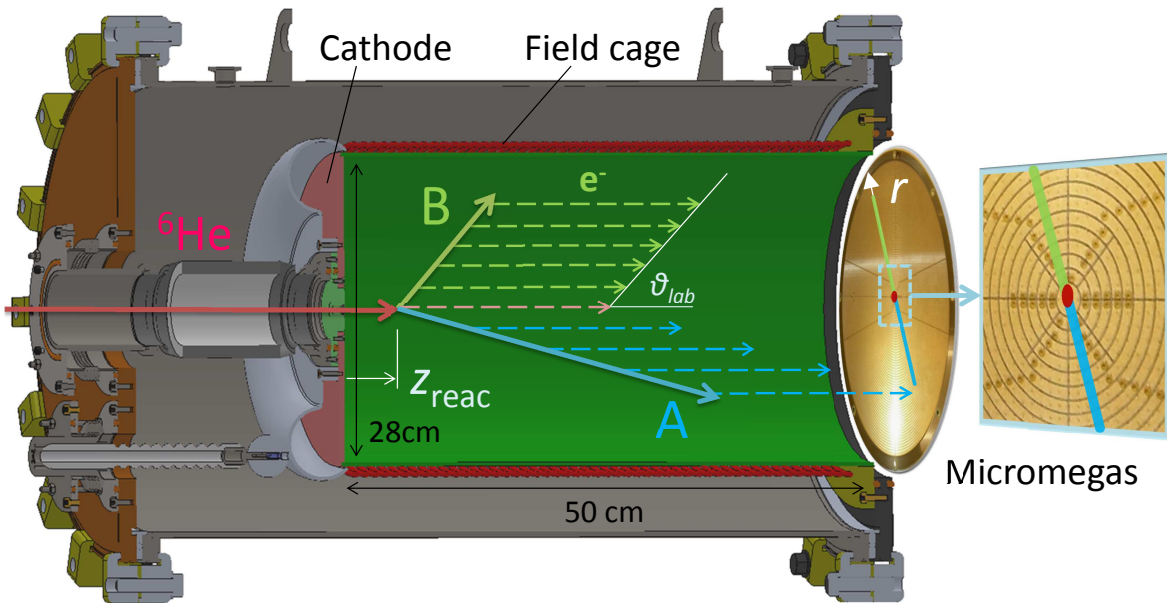
FIG. 1. (Color online) Schematic drawing of the experimental setup of the PAT-TPC. The inset is a magnified view of the segmented anode pad plane of the Micromegas detector near the beam axis.

The PAT-TPC was installed 1.5 m downstream of the end of *TwinSol*. A schematic drawing of the setup is shown in Fig. 1. The detector encompasses a cylindrical field cage of 50 cm in length and 28 cm in diameter, which is centered on the beam axis. The cage was filled with a He:CO_2 90:10 mixture gas at atmospheric pressure, which serves simultaneously as the tracking medium as well as the reaction target containing ^{4}He. To limit impurities, the gas was kept continuously flowing at a rate of 4.5 cm^3/s, which replaces the whole volume of gas every 2 hours. The ^{6}He particles entering through an entrance window travel down along the symmetry axis of the field cage and induce nuclear reactions with the gas nuclei. Both the beam particles and outgoing charged particles from the reactions ionize gas atoms while traveling across the gas volume. Their paths are reconstructed from the ionization electrons, which are transported downstream by an electric field parallel to the beam axis, and multiplied by the gas electron amplifier, Micromegas [44]. The latter was fabricated by the SEDI/IRFU, CEA-Saclay. An electric field of 0.8 kV/cm was generated by a negative potential of -40 kVDC applied to a cathode plate at the upstream end of the cage. The initial potential was stepped down by a series of equipotential rings toward the Micromegas. The resulting electron drift velocity was measured to be about 2.4 cm/μs [43]. The field cage is gas tight and is surrounded by nitrogen gas at atmospheric pressure, which provides a high dielectric strength to mitigate the risk of discharge to the chamber walls at ground potential.

The secondary beam was focused on the entrance window of the PAT-TPC. The spot size of the ^{6}He beam at the window was estimated to be 25 mm in diameter from solenoid optics calculations, while the entrance aperture is circular with a diameter of about 8 mm. The beam was thus collimated by the window, which changed the intensity and purity of ^{6}He in the TPC. These quantities were estimated using signals from the micromesh of the Micromegas, of which a detailed description is given later. The ^{6}He particles are decelerated in the gas and stop at the end of the field cage about 50 cm downstream of the beam window, fully depositing 15 MeV of energy. In contrast, ^{4}He has higher energy and punches through the TPC while losing only 6 MeV in the detector volume. This results in a pulse-height difference in the micromesh signals, thus allowing identification and counting of the respective nuclei. The average intensity of the collimated ^{6}He beam was 2×10^3 counts per second with a purity of 90% at a primary ^{7}Li(3$^+$) beam intensity of 0.5 electric μA.

The Micromegas consists of an anode readout plane and a micromesh stretched over it.

Electron avalanches occur in the narrow amplification gap of 128 μm defined by the anode and the micromesh. The micromesh was biased at -320 V to create a high field gradient over the gap, while the anode plane was grounded. The gas gain was measured to be about 75 as also reported elsewhere [43]. The anode plane of the Micromegas has a circular-shaped active area of 250 mm in diameter. It is segmented into multiple pads to read out and locate the avalanche electrons. Specifically, the anode pads consist of a 5-mm-diameter central pad and 2-mm-pitch coaxial strips, each spaced by a gap of 0.25 mm (inset of Fig. 1). The coaxial strips are divided into quadrants and the five innermost strips into octants. The beam particles travel approximately perpendicular to the anode plane. The central pad and its neighboring coaxial strips record the energy deposit profile as a function of time, and the position along the beam axis (z) is deduced from the drift time of ionization electrons. The particles emitted from a reaction travel away from the center to the perimeter. Each particle traverses a series of coaxial strips in a given quadrant. This set of strips thus gives the energy deposit profile as a function of the radius r of the strip as well as z, providing the polar angle and the range of the reaction products. Examples of energy deposit profiles are found in our previous report [43].

A total of 253 signals from the anode plane were read out by a combined preamplifier/shaper/wave-digitizer system developed for the neutrino-flux monitor of the T2K experiment [45, 46], which is referred to as T2K electronics hereafter. The T2K electronics were set to record the waveform of input signals at 12.5 MHz over the full time range of 40 μs. A time bin width thus corresponds to 80 ns, or a spatial size of 2 mm along the beam axis given the electron drift velocity of 2.4 cm/μs. To generate external triggers for the T2K electronics, signals from the micromesh as well as from some coaxial anode strips were routed to an auxiliary circuit consisting of NIM-standard modules. Two sets of data were taken with different triggers. The first trigger was optimized for the elastic and inelastic scattering of ^{6}He on α particles. The primary signature of these reactions is the observation of two helium isotopes, ^{4}He and/or ^{6}He, involved in the final state. Because of the low atomic number ($Z = 2$), both particles have a long range and traverse many strips away from the center. The trigger was thus designed to record events which fire specific off-center strips in different quadrants. The four coaxial strips, each belonging to different quadrants, located at a radius of 18 mm were used as trigger sources. The data acquisition was triggered on tracks that extend 18 mm or more in radius in two or more quadrants. For monitoring

8

purposes, the trigger from one quadrant, or multiplicity equal to one, was also added after downscaling by a factor of 32. The second trigger was used to record ^{6}He + α reactions involving beryllium in the final state. These reactions produce a large energy deposit in a short distance due to the high Z of Be and its low recoil velocity. The time structure of the micromesh signal was used to generate a trigger when the signal had (a) a higher Bragg peak and (b), later times with respect to the Bragg peak of the fully stopped ^{6}He beam. The late times imply that the observed Bragg peak is located closer to the beam entrance, making it a good indicator of the occurrence of a reaction during the deceleration of the beam. The average rate of Trigger 1 was 15 Hz, while that of Trigger 2 was 50 Hz. The live-time ratio of the data acquisition was 70% and 40%, respectively, for these two triggers.

III.   ANALYSIS

A.   Elastic and inelastic scattering

In the following section, we describe the analysis procedure of the elastic and inelastic scattering data taken with Trigger 1 (optimized for these processes). Part of the analysis procedure, particularly the tracking of the ^{6}He beam and reaction products (^{6}He and/or ^{4}He), is the same as reported in Ref. [43]. Energy deposition was calculated using the SRIM code [47].

The total kinetic energy (TKE) and the emission angle (θ_{lab}) of reaction products were obtained by analyzing the set of information on charge Q_i, radial position r_i and signal timing t_i from the coaxial strips, denoted by i, which the particle tracks traveled over. First, the angle θ_{lab}, which is defined with respect to the beam axis, or the axis of time projection (Fig. 1), was determined from the slope of the t $vs.$ r plot. A linear fitting function was adopted and defined as:

$$t = \frac{r}{v_{\mathrm{drift}} \tan \theta_{\mathrm{lab}}} + t_1 \tag{1}$$

with v_{drift} being the electron drift velocity and t_1 the time at $r = 0$. Once θ_{lab} was determined from the fit, the Q $vs.$ r plot, which represents the energy deposition profile in the radial direction, was compared to calculated curves at a given TKE using the θ_{lab} previously obtained. The optimal TKE was determined to minimize χ^2 with respect to the experimental data. Some of the particles escaped from the active volume of the PAT-TPC, particularly

9

the ones with large or small scattering angles where the energies are higher. To obtain the acceptance over a wide angular range, we also analyzed the events involving particle escapes. While the range cannot be determined for these particles due to the missing position information of the Bragg peak, the amplitude and slope of the energy deposit profile towards the Bragg peak are still sensitive to the TKE, which allows TKE determination by the same χ^2 minimization procedure. The quality of the TKE determination of escaping particles will be discussed later when the reconstruction of the excitation energy spectrum of ^{6}He is presented. When a given particle stops inside the active volume, ^{6}He and α particles can be differentiated from the amplitude of the tail of Bragg peak as demonstrated in our previous report [43]. In the present analysis, however, we differentiated ^{6}He and ^{4}He from the reaction kinematics as detailed later.

Reconstruction of reaction kinematics by the missing mass method requires knowing the energy of the beam particles. In the present measurement, the energy continuously decreases as the beam particle travels along the beam axis. To determine the reaction energy, the energy deposition before reaching the reaction position (z_{reac}) needs to be taken into account. In this analysis, z_{reac} was determined from the recorded drift times of ionization electrons released at the positions of the reaction vertex and the beam entrance. The drift time corresponding to the reaction position was given by that of the reaction vertex t_1 previously deduced in the analysis of the trajectory of the reaction products. The drift time of electrons released at the entrance (t_0) was obtained by analyzing the waveform of anode signals near the central region, which represents the energy deposit profile of beam particles along the beam axis. The anode signals of the central pad and its neighboring coaxial strips were summed when the beam charge spreads over multiple pads. The difference between the two times $t_0 - t_1$ was then translated into z_{reac} using the electron drift velocity. The corresponding energy loss was calculated and subtracted from the initial beam energy to define the energy at the moment of the reaction (E_{reac}).

The ^{6}He ions and the contaminant ^{4}He ions in the secondary beam were differentiated from the energy deposit per unit length (dE/dz) averaged over the track from t_0 to t_1. The value of dE/dz provides a good measure of isotope separation as the ^{6}He particles have lower energies (3.8 MeV/u or less) compared to the ^{4}He contaminants (4.4−5.6 MeV/u). Figure 2(a) shows the scatter plot between dE/dz and z_{reac}, where two loci corresponding to ^{6}He and ^{4}He are clearly separated. The separation of the loci, which becomes smaller at

10

shorter travel lengths, is uncertain below $z_{\text{reac}} = 50$ mm, where the finite value of the shaping time (0.5 μs) smears the difference in dE/dz. In this region, the properties of the reaction kinematics were further used to eliminate elastic scattering events of ^{4}He on α particles. A gate was set on the sum of the angles $\theta_{\text{lab}}^{(i)}$ of the two reaction products labeled $i = 1$ and 2. Figure 2(b) shows the $\theta_{\text{lab}}^{(1)} + \theta_{\text{lab}}^{(2)}$ $vs.$ dE/dz plot for the region of $z_{\text{reac}} < 50$ mm. A cluster is seen at 90 degrees. This corresponds to ^{4}He beam scattered by the ^{4}He in the gas. The opening angle of two identical particles from elastic scattering always equals 90 degrees in the laboratory frame regardless of the center-of-mass scattering angle. The gate displayed in the figure was adopted to exclude these ^{4}He-beam events.
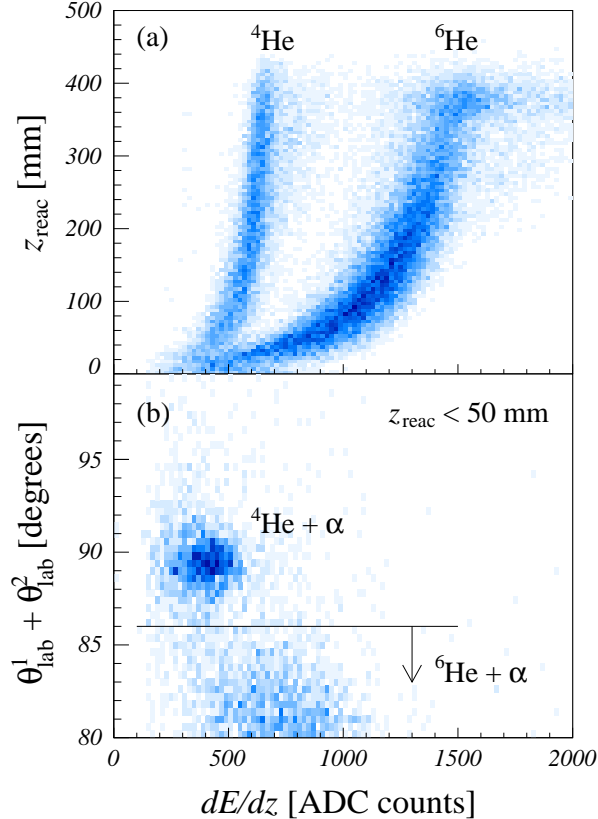
FIG. 2. (Color online) Identification of the secondary beam particles. (a) Scatter plot between the energy loss per unit length of beam path dE/dz and the reaction position z_{reac}. (b) Scatter plot between dE/dz and the opening angle of reaction products $\theta_{\text{lab}}^{(1)} + \theta_{\text{lab}}^{(2)}$ for the events at $z_{\text{reac}} < 50$ mm. The gate to select ^{6}He scattering is indicated.

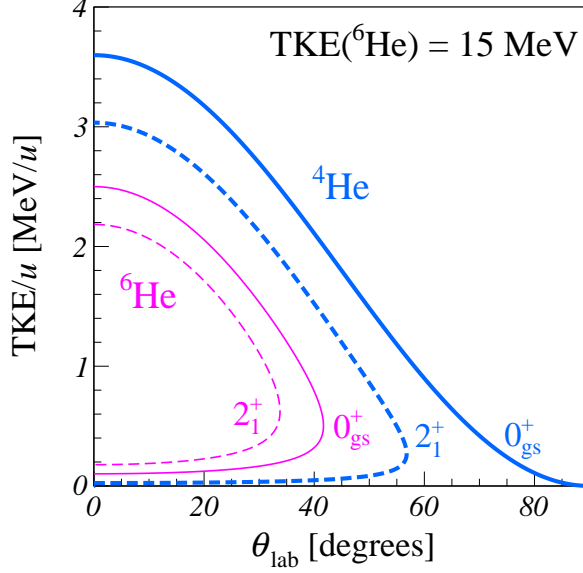The excitation energy of ^{6}He (E_{x}) and the center-of-mass scattering angle ($\theta_{\text{c.m.}}$) were

11

FIG. 3. (Color online) TKE/u $vs.$ θ_{lab} plot for ^{6}He + α scattering at 15 MeV. Elastic scattering and inelastic scattering to the first 2^+ state of ^{6}He are denoted by the solid and dashed lines, respectively. Calculated curves are shown both for the recoiling α (thick blue) and scattered ^{6}He (thin magenta) particles.

obtained by the missing-mass method using E_{reac} as well as TKE and θ_{lab} of the recoiling α particles. An inherent issue in deducing excitation-energy spectra from ^{6}He + α-particle scattering is that another α particle is produced in the final state when inelastically scattered ^{6}He decays via $2n$ emission. All excited states of ^{6}He are unbound above the $2n$ separation energy at 0.972(1) MeV [48]. It is therefore necessary to correctly select the α particle recoiling from the target. The information on kinematical properties of the reaction was used to eliminate the ambiguity in identifying the recoiling particle. Figure 3 shows the calculated plots of TKE per nucleon (TKE/u) $vs.$ θ_{lab} for elastic and inelastic scattering to the 2^+ state at a beam energy of 15 MeV. It is found that TKE/u, or the velocity of ^{6}He, is always smaller than that of the recoiling α particle at a given laboratory angle except for the very forward region below 10 degrees in the center-of-mass frame, which is outside the present detector acceptance. Therefore, the range of the α particle following $2n$ emission decay tends to be shorter than that of the recoiling α particle. According to these characteristics, we adopted the following procedure. First, two excitation energies $(E_{\text{x}}^{(i)})$ were obtained individually from two reaction products by assuming the particle i as

12

the recoiling α particle. The set of $E_x^{(i)}$ were then compared. If the ^{6}He particle, or the α particle after $2n$ emission decay, is identified as the recoiling α particle, its shorter range results in an underestimate of TKE and thus gives higher excitation energies than the true value. Accordingly, we adopted the particle with a smaller E_x as the recoiling α particle.
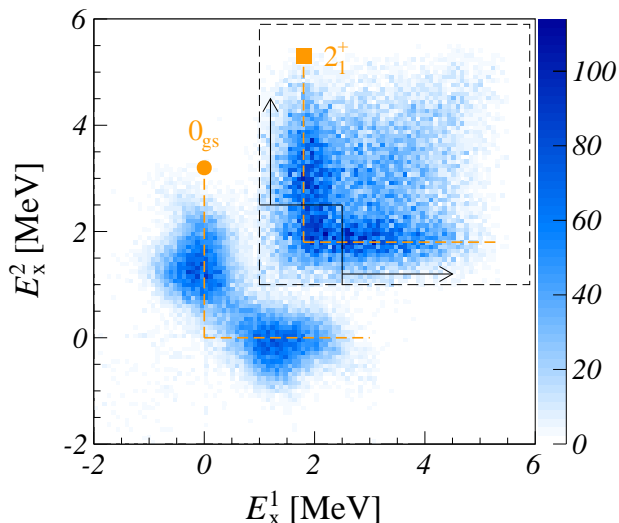
FIG. 4. (Color online) Scatter plot between $E_x^{(1)}$ and $E_x^{(2)}$. The events to the left of the solid lines were excluded from the analysis. The contents of the region inside the dashed lines are weighted by a factor of 3 for presentation purposes.

Figure 4 shows the scatter plot between $E_x^{(1)}$ and $E_x^{(2)}$, where the indices 1 and 2 were randomly assigned. Loci corresponding to the ground state and the first 2^+ state at 1.79 MeV are visible. It is evident in the locus of elastic scattering that the smaller $E_x^{(i)}$ value of a given pair is mostly found near 0 MeV and well separated from the larger $E_x^{(i)}$ which is wrongly estimated from the scattered ^{6}He. The result is similar for the 2^+ state, of which the locus appears above 1.9 MeV only. However, the separation in the region close to the $E_x^{(1)} = E_x^{(2)}$ line is not as clear as that of the ground state because of the velocity shift due to particle emission and the contribution of breakup events. Therefore, above $E_x = 1$ MeV, the events with $E_x^{(1)}$ and $E_x^{(2)}$ <2.5 MeV were eliminated from the analysis to ensure a sufficient difference in energy for properly selecting α particles.

The resulting excitation-energy spectrum of ^{6}He is shown in Fig. 5(a). Two peaks visible near 0 and 2 MeV correspond to the 0^+ ground state and the first 2^+ state at
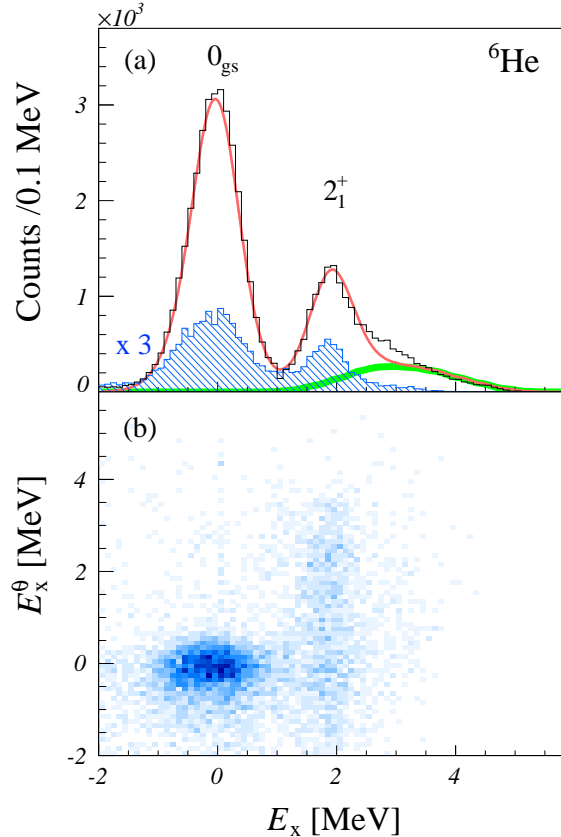
FIG. 5. (Color online) (a) Excitation-energy spectrum of ^{6}He (unshaded histogram). The best-fit result (thin red line) is shown together with the contribution of the background from the ^{6}He breakup reaction (thick green line). The spectrum in the shaded histogram was made by selecting backward scattering ($\theta_{\text{c.m.}} > 90°$) with particle escape from the TPC. (b) Scatter plot of E_x and E_x^θ. E_x^θ is the excitation energy of ^{6}He obtained from the angles of the two reaction products.

1.797(25) MeV [49]. A fit to the spectrum gives excitation energies of $-0.01(1)$ and 1.90(1) MeV, respectively, where the quoted errors are statistical. The FWHM resolution is about 0.85 MeV. The fitting function consisted of a Gaussian function for the ground state, a Voigt function [50] for the unbound 2^+ state, and background from the breakup reaction of ^{6}He involving the final state of an α particle and 2 neutrons. The Voigt function is a convolution of a Breit-Wigner function and a Gaussian, which allows the natural width of an unbound state and the resolution of the detection system to be taken into account. The width of the 2^+ state was set to the adopted value, 0.113(20) MeV [49]. The background shape was simulated by the Monte-Carlo method, where the α particle and neutrons in the

14

final state were generated in a uniform phase space. The procedure of identification based on the comparison between a pair of $E_\mathrm{x}^{(i)}$ was taken into account. The best-fit curve shown in the figure well reproduces the experimental data. The background of the breakup reaction denoted by the thick line accounts for the tail towards higher energies.

In the present analysis, TKE for an input to the missing-mass method was deduced from the slope of the Bragg curve when recoiling α particles escape from the active region and hence the Bragg peak is unavailable. Without the precise position information of the Bragg peak, the analysis might result in inaccurate excitation energies. The gated spectrum for one-particle escape events is shown in the shaded spectrum of Fig. 5(a). The spectrum clearly shows a two peak structure, confirming good reconstruction of the reaction kinematics. To further confirm the results, the adopted excitation energies are compared to excitation energies (E_x^θ) that were obtained from the correlation of laboratory angles, $\theta_\mathrm{lab}^{(1)}$ and $\theta_\mathrm{lab}^{(2)}$, between the two reaction products. This method does not require the knowledge of the TKE of reaction products. Thus we can correctly extract excitation energies from the escape events as long as the scattered ^{6}He particle is stable against particle emission and keeps its initial angle unchanged after scattering. The scatter plot of E_x^θ against E_x is shown in Fig. 5(b). A gate was set to select backward scattering angles of $\theta_\mathrm{c.m.} > 90$ degrees, where most of the escaping particles are recoiling α nuclei. The presence of a cluster centered at $E_\mathrm{x}^\theta = E_\mathrm{x} = 0$ MeV indicates that most of the events involving the ground state have E_x well correlated with E_x^θ. The ratio of the number of events in the cluster is nearly 90% with respect to that of the peak in the shaded spectrum in Fig. 5(a), limiting the systematic uncertainty in yields to 10%. The locus for the 2^+ state widely spreads along the vertical axis of E_x^θ because the angles of scattered particles shift after the $2n$ emission.

B. Two-neutron emission channel

To investigate branching to the two-neutron emission ^{6}He$(\alpha, 2n)^8$Be channel, the trigger was set for reactions having a peak in the energy loss profile which was taller than the Bragg peak of the ^{6}He beam particles (Trigger 2). In the data analysis a peak was observed for Bragg amplitudes that corresponded closely to 4.5 MeV mg^{-1} cm^2, the value expected for two highly-correlated α particles, such as originating from the decay of ^{8}Be. Since this amplitude is lower than 5.9 MeV mg^{-1} cm^2 for ^{9}Be ions with a higher Z recoiling from
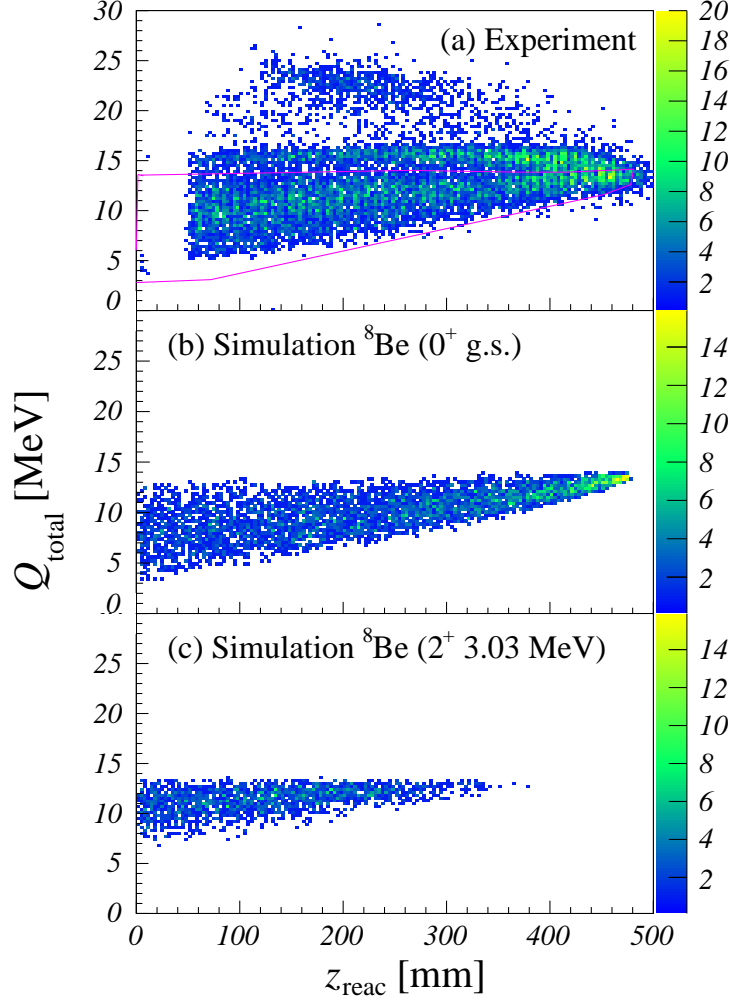
15

FIG. 6. (Color online) Total charge collected Q_{total} as a function of the location of the reaction vertex z_{reac}. (a) Experimental data. The elastic events are clearly distinguishable near $Q_{\text{total}} = 15$ MeV. Events above the locus of elastic scattering indicate pile up of beam particles. Only events inside the contour line were used in calculating the excitation function. (b) Simulated results for the decay into the 0^+ ground state and (c) the 2^+ state at 3.03 MeV of ^{8}Be.

the ^{6}He$(\alpha, n)^9$Be reaction, we concluded the main decay channel that contributed was ^{10}Be $\rightarrow 2n + {}^8$Be, with ^{8}Be unbound to α decay by 92 keV. Beam contaminants were eliminated offline by comparing the particle's energy loss profile near the beginning of its track to the experimentally-measured energy-loss profile for ^{6}He. The location of the reaction vertex z_{reac} was determined from the time where the enhancement of the energy deposits starts due to the creation of reaction products. Since the beam particles and the charged

16

reaction products were stopped in the detector, we could use the total charge collected in the detector (Q_{total}) as the energy sum signal, which was obtained by summing all anode signals. Q_{total} is plotted as a function of the location of the reaction vertex z_{reac} in Fig. 6(a). The total charge is converted to energy by normalizing the experimental data to the allowed energies from a kinematical simulation of the sequential decay of $^{10}\text{Be} \rightarrow 2n + {}^{8}\text{Be} \rightarrow 2n + 2\alpha$ described later. The events shown are selected by the Bragg amplitude for two-α correlated events. The events in the $z_{\text{react}} < 50$ mm region were rejected because it was difficult to distinguish ^{8}Be events from beam contaminants, particularly ^{7}Li, when the incident energy loss curve was relatively short. As can be seen in Fig. 6(a), there is an accumulation of events near 15 MeV for the charge collected for full beam energy deposition corresponding to elastic scattering. Below this line is a broad range of energies deposited in the detector. These events are attributed to the $^{6}\text{He}(\alpha, 2n)^{8}\text{Be}$ reaction since the neutrons were not detected in our experiment and the energy taken away by them will be missing in the total energy signal. We simulated events corresponding to the decay of ^{10}Be into ^{8}Be with the unobserved two neutrons, for which we assumed isotropic emission in the center-of-mass system and phase-space sharing of the available energy between the two neutrons. It is also assumed that the decay of $^{10}\text{Be} \rightarrow 2n + {}^{8}\text{Be} \rightarrow 2n + 2\alpha$ is sequential. The decay into the 2^{+} state at 3.03 MeV of ^{8}Be, which is energetically allowed at higher energies, is simulated as well. The results for the ground state and the 2^{+} state are shown in Fig. 6(b) and (c), respectively. The kinematical simulation for the ground state is seen to agree well with the data, confirming the interpretation of the events. The simulation also served as a guide for defining the contour line seen in Fig 6(a). Only the events inside the contour line were subsequently used to calculate the excitation function.

IV. RESULTS

A. Elastic and inelastic scattering

To obtain excitation functions and angular distributions, cross sections ($d\sigma/d\Omega$) were deduced for a given bin of the reaction position z_{reac}^{i} and the scattering angle $\theta_{\text{c.m.}}^{j}$ specified by the indices (i, j), respectively. Yields ($Y^{(i, j)}$) of the ground state and the 2^{+} state were obtained by fitting excitation energy spectra using the same function as adopted for the fit

17

to the angle-integrated spectrum of Fig. 5(a). $Y^{(i, j)}$ was then translated into $d\sigma/d\Omega^{(i, j)}$ following the expression:

$$d\sigma/d\Omega^{(i, j)} = Y^{(i, j)}/\left(\epsilon_{eff}^{(i, j)} \cdot \epsilon_{\mathrm{DAQ}} \cdot N_{^6\mathrm{He}} \cdot N_{\mathrm{He}}^{(i)} \cdot \Delta\Omega^{(j)}\right), \quad (2)$$

where the indices i and j denote that the associated parameter depends on z_{reac} and $\theta_{\mathrm{c.m.}}$, respectively. The detection efficiency $\epsilon_{eff}^{(i, j)}$ was estimated by simulations, where the geometries of the detector, the condition of the trigger, and the energy losses of beam and reaction products were taken into account. The live-time ratio of the data acquisition ϵ_{DAQ} was 70% on average. The integrated count of ^{6}He beam particles $N_{^6\mathrm{He}}$ was estimated using the counts of micromesh signals measured by a scaler. This was about 2×10^8 after taking into account the beam purity of 90%. The number of He atoms in the gaseous target $N_{\mathrm{He}}^{(i)}$ was calculated from the density of the He:CO$_2$ 90:10 gas at atmospheric pressure (0.33 mg/cm^3) and the bin size of z_{reac}. The solid angle $\Delta\Omega^{(j)}$ was calculated from the bin size of $\theta_{\mathrm{c.m.}}$.

The resulting excitation functions for elastic scattering are shown in Fig. 7. The beam energy in the laboratory frame, E_{reac}, was converted into the center-of-mass energy by $E_{\mathrm{c.m.}} = 0.4 \times E_{\mathrm{reac}}$. Given the separation threshold of an α particle at 7.42 MeV [48], $E_{\mathrm{c.m.}}$ is related to the excitation energy in ^{10}Be by $E_{\mathrm{x}} = E_{\mathrm{c.m.}} + 7.42$ MeV. The systematic error of $E_{\mathrm{c.m.}}$ is estimated to be ± 0.1 MeV, which arises from the deviation of E_{reac} with respect to the energy sum of the ^{6}He and α particles from elastic scattering. A strong enhancement of cross sections is observed around 2.7 MeV in the angle-integrated spectrum of $\theta_{\mathrm{c.m.}} = 65°-135°$ in Fig. 7(a). A peak consistently exists around this energy in the different angular regions shown in Figs. 7(b)$-$(h), indicating the presence of a resonance. A fit with a Voigt function [50] and a linear background gives a resonance energy of $E_{\mathrm{c.m.}} = 2.57(15)$ MeV, where the quoted uncertainty is the sum of the statistical and systematic errors. This is consistent with the resonance of the state at $E_{\mathrm{x}} = 10.15(2)$ MeV, or $E_{\mathrm{c.m.}} = 2.73(2)$ MeV, observed in a previous measurement of elastic scattering [32]. No peak is visible in the excitation functions except for this strong resonance. The absence of sizable resonances indicates that no other states have a large decay width for α emission within the energy window of the present study ($E_{\mathrm{c.m.}} = 2 - 6$ MeV).

The excitation functions for inelastic scattering are shown in Fig. 7. A sizable decay width to the 2^+ state of ^{6}He was inferred for the 2.73-MeV resonance in the analysis of the previous study [32]. However, this could not be measured in the present study due to
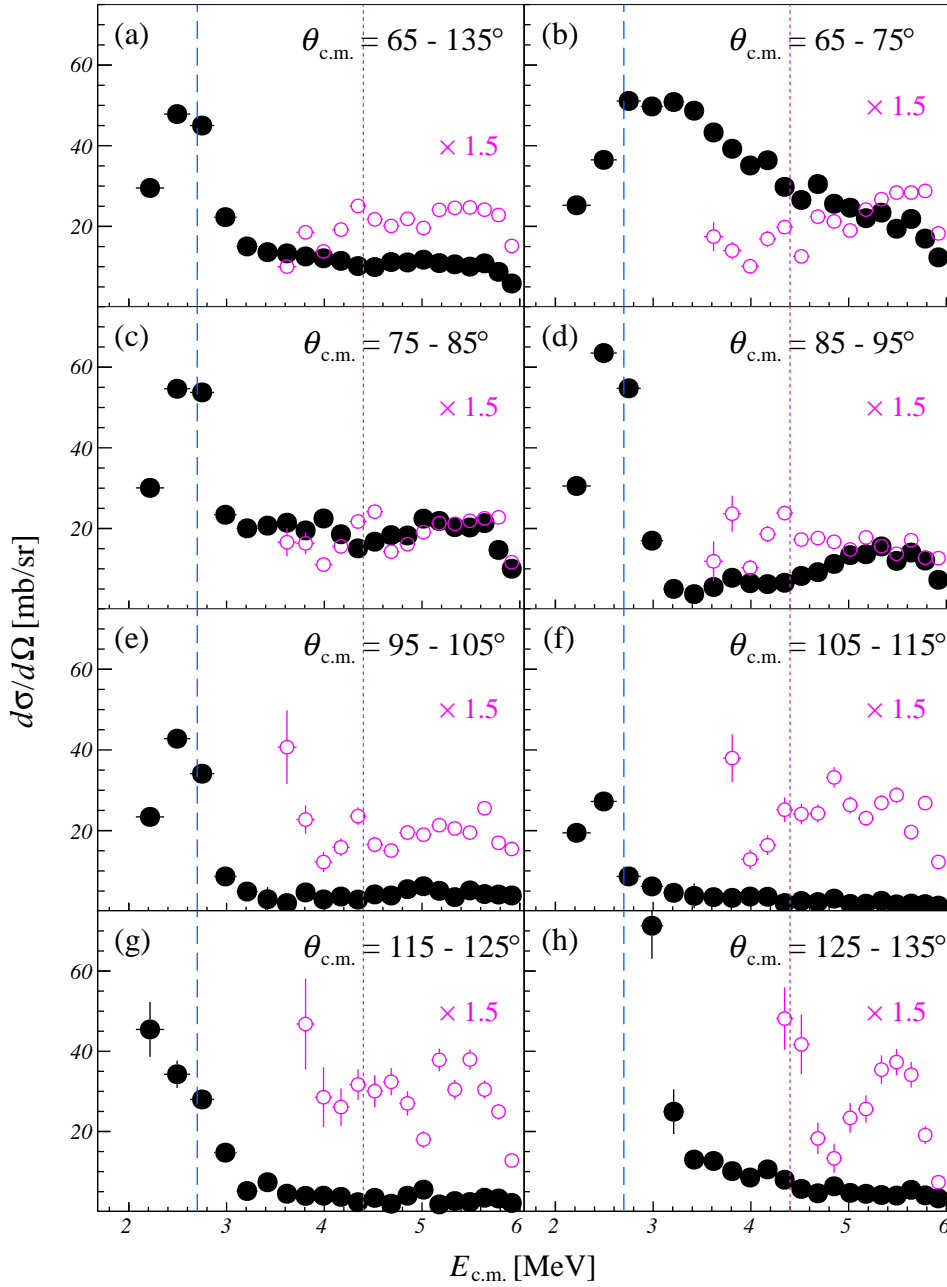
18

FIG. 7. (Color online) Excitation functions of ^{6}He + α scattering: (a) angle-integrated spectrum over $\theta_{\text{c.m.}} = 65° - 135°$, and (b−h) spectra for $10°$ angular bins. The data for elastic scattering are shown by the filled circles, while those for inelastic scattering to the 2^+ state are shown by the open circles. The inelastic scattering data are scaled by a factor of 1.5. The dashed and dotted lines denote $E_{\text{c.m.}} = 2.7$ and 4.4 MeV, respectively.
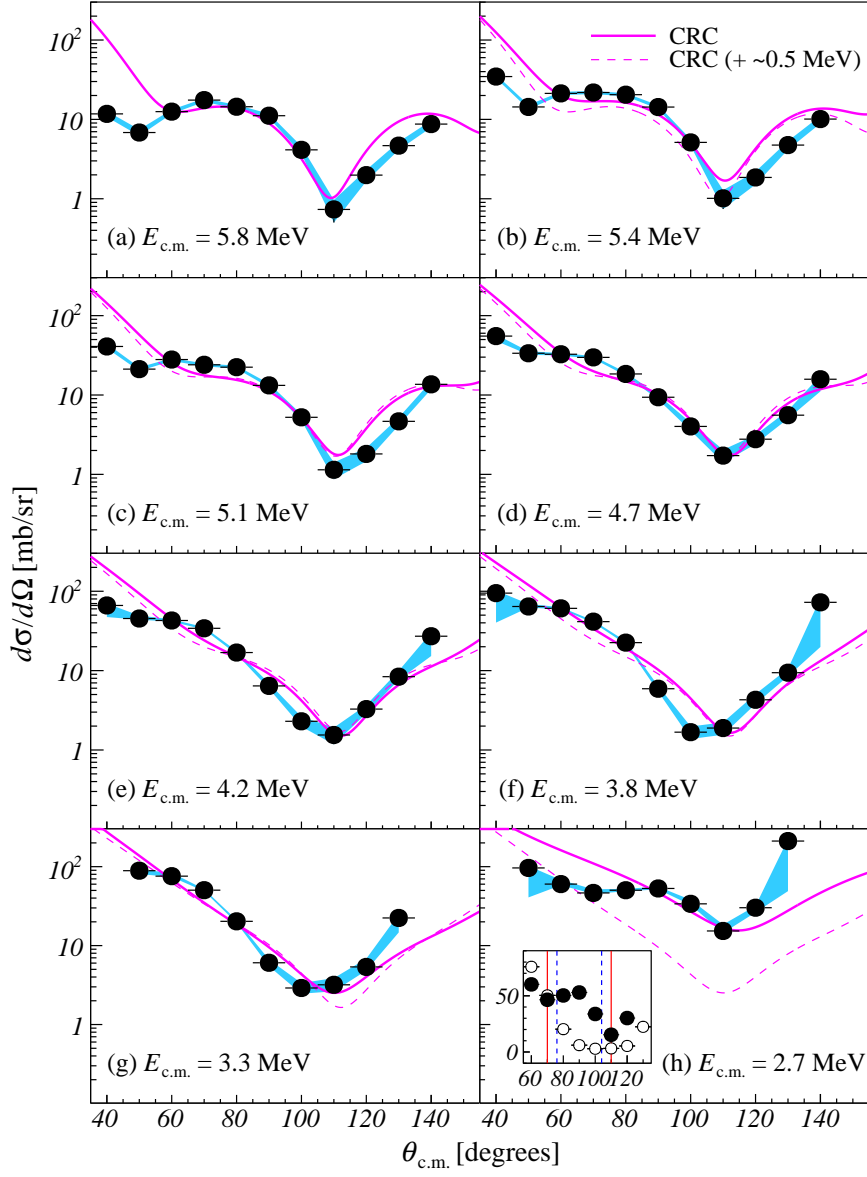
FIG. 8. (Color online) Angular distributions of elastic ^{6}He + α scattering. The results of CRC calculations (solid lines) are compared to the data. The CRC results at the higher energy bins are also shown for reference with the dashed lines. The blue shaded areas denote the systematic errors from the ambiguities in the beam angle. The inset (h) shows the data at $E_{\text{c.m.}} = 2.7$ (full circles) and 3.3 MeV (open circles) on a linear scale. The angles where the Legendre polynomials $P_L(\cos\theta_{\text{c.m.}})$ for $L = 4$ and 6 become zero are denoted by the solid and dashed lines, respectively.
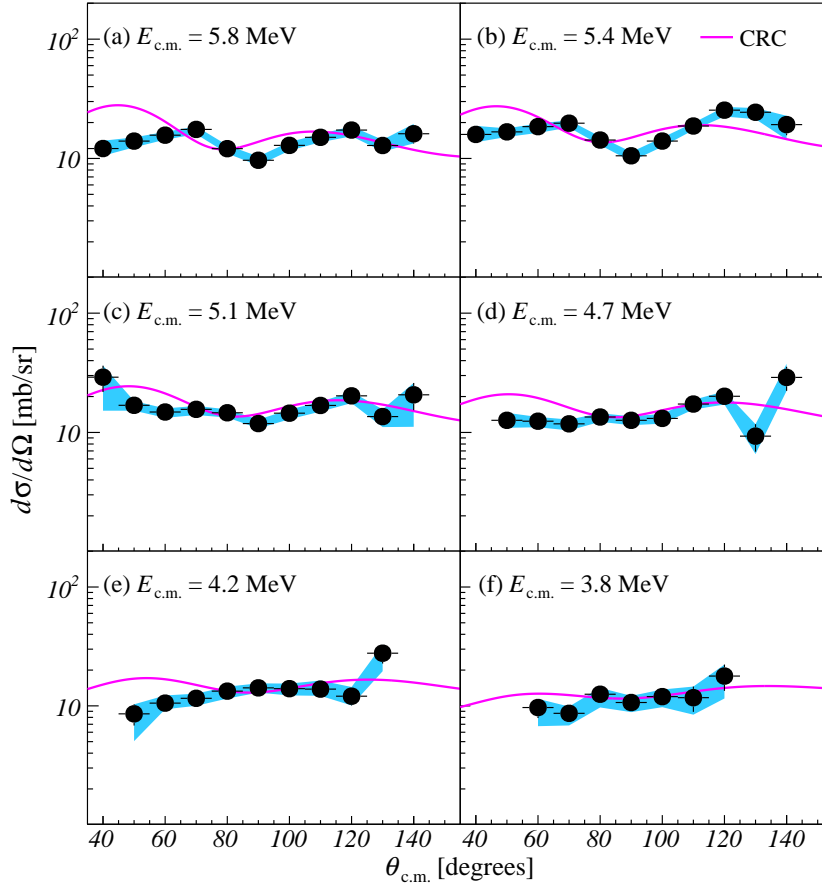
FIG. 9. (Color online) Angular distributions of inelastic ^{6}He $+ \alpha$ scattering to the ^{6}He 2^+ state. The results of CRC calculations (solid lines) are compared with the data. The blue shaded areas denote the systematic errors from the ambiguities of the beam angle.

the lack of acceptance at this energy. While there are no resonances as strong as the one observed in the elastic channel, a small peak is visible at 4.4 MeV in the inelastic channel consistently over the angular region of $\theta_{c.m.} = 65°-105°$, which might be due to a resonance.

The differential cross sections were deduced for eight different incident energies to study angular distributions. The resulting data for elastic scattering are displayed in Fig. 8. The vertical error bars are only statistical, and the horizontal bars denote the size of the angular bins. The leading contributions of the systematic error are the uncertainty of yields for the escape events (10%) and the detection efficiency. The latter mostly comes from the uncertainties of the beam angle, which could be inclined by about 1 degree with respect to the central axis. The blue shaded areas in Figs. 8 denote the variation of cross sections when

the incident beam angle varies by 1 degree. As seen in the figures, a series of differential cross sections for elastic scattering show a gradual and continuous change in their angular distributions as a function of $E_{\text{c.m.}}$ until the cross sections are enhanced at $E_{\text{c.m.}} = 2.7$ MeV. In the inset of Fig. 8(h), the on-resonance data at $E_{\text{c.m.}} = 2.7$ MeV (filled circles) are compared to the off-resonance data at $E_{\text{c.m.}} = 3.3$ MeV (open circles) shown on a linear scale. At $E_{\text{c.m.}} = 2.7$ MeV, the cross section clearly peaks at $90°$ and dips at $60°$ and $110°$. In contrast, the data at $E_{\text{c.m.}} = 3.3$ MeV lack such a steep rise and drop, indicating that the peak and dip structures seen in the 2.7-MeV data are due to the resonance. Angular distributions of resonance scattering primarily follow the square of the Legendre polynomial $[P_L(\cos\theta_{\text{c.m.}})^2]$ corresponding to the angular momentum (L) involved. The diffractive pattern observed is therefore a useful measure to identify L. The presence of a peak at $90°$ rules out the odd angular momenta, of which the corresponding Legendre polynomials always become zero at this angle. The dips at $70°$ and $110°$ more agree with the polynomial of $L = 4$ than that of $L = 2$ having zeros at $55°$ and $125°$, or $L = 6$ at $76°$ and $104°$. The dip angles of $L = 4, 6$ are shown for reference by the solid and dashed lines, respectively, in the inset of Fig. 8(h). The diffractive pattern of the experimental data is seen closer to that of $L = 4$ and clearly deviated from that of $L = 6$ despite the larger angular bins and the lower statistics compared to a previous measurement [32]. We therefore assign $L = 4$ for the resonance observed. Since the initial and final states involve spinless particles only, the spin-parity of the corresponding resonant state in ^{10}Be is assigned as 4^+. The present results thus confirm the resonance of the 4^+ state at $E_{\text{x}} = 10.15$ MeV in ^{10}Be observed in a previous measurement of elastic ^{6}He + α scattering [32], and rule out the spin-parity of 3^- claimed in an angular correlation study using the ^{7}Li + ^{6,7}Li reactions [30]. The angle-integrated cross section ($\sigma_{4\pi}$) can be translated into the partial α decay width (Γ_α) via the relation [52]:

$$\sigma_{4\pi} = (2L + 1)\frac{\pi}{k^2}\frac{\Gamma_\alpha^2}{(E_{\text{c.m.}}^0 - E_{\text{c.m.}})^2 + (\Gamma/2)^2}, \tag{3}$$

with k being the wavenumber, $E_{\text{c.m.}}^0$ the resonance energy, and Γ the total decay width. The total width of 296(15) keV measured in a previous study [30] was adopted for Γ. $\sigma_{4\pi}$ was estimated from the cross section of the resonance in the angular range $\theta_{\text{c.m.}} = 65° - 135°$ in Fig. 7(a) given the $P_4(\cos\theta_{\text{c.m.}})^2$ dependence of the angular distribution. The resulting ratio of Γ_α/Γ is 0.49(5), which corresponds to $\Gamma_\alpha = 145(15)$ keV. This Γ_α/Γ ratio agrees with 0.45(3) from the previous study [32].

22

TABLE I. Best-fit values of the optical model potential parameters and the $\langle ^6\mathrm{He}|^4\mathrm{He} + 2n\rangle$ overlap spectroscopic factor. See text for details.

$E_{\text{c.m.}}$ (MeV)	N_{R}	$W(r)$ (MeV)	r_W (fm)	a_W (fm)	$\mathrm{SA}_{\text{g.s.}}$
5.82	1.0	60.0	1.26	0.27	0.80
5.45	1.0	60.0	1.27	0.25	0.80
5.06	1.0	60.0	1.27	0.25	0.80
4.64	1.0	60.0	1.27	0.25	0.80
4.21	1.0	60.0	1.27	0.25	0.80
3.76	1.0	60.0	1.28	0.25	0.80
3.26	1.0	65.0	1.28	0.32	0.80
2.69	1.0	65.0	1.38	0.20	0.80

To assess the contribution of direct reactions, coupled reaction channels (CRC) calculations were performed using the code FRESCO [53]. These calculations are similar to those of Khoa and von Oertzen [40], although some simplifications were made in light of their results. We adopted the same basic model as Ref. [40] for the optical potentials, i.e. a double-folded real potential and a Woods-Saxon imaginary potential, giving a potential of the form:

$$U(r) = N_{\text{R}}V_{\text{DF}}(r) + iW(r) + V_{\text{C}}(r), \qquad (4)$$

where $V_{\text{C}}(r)$ is the usual Coulomb potential with radius $R_{\text{C}} = 1.25(A_1^{1/3} + A_2^{1/3})$ in fm, $V_{\text{DF}}(r)$ is the double-folded real potential with normalization parameter N_{R} and $W(r)$ is the imaginary potential of depth W in MeV, radius $R_{\text{W}} = r_W(A_1^{1/3} + A_2^{1/3})$ in fm and diffuseness a_W in fm. The parameters N_{R}, $W(r)$, r_W and a_W were adjusted to obtain the best agreement with the data at each energy. The double-folding potentials were calculated with the code DFPOT [54] using the M3Y effective interaction [55]. The ^{4}He nuclear-matter density was derived from the three-parameter Fermi distribution charge density of Ref. [56] by unfolding the proton charge distribution as described in Ref. [57], assuming that $\rho_n = (N/Z)\rho_p$, and the ^{6}He nuclear-matter density was the FC6 model density of Ref. [58]. Inelastic excitation of the 1.8-MeV 2^+ state of ^{6}He was included in a similar way as detailed in Ref. [40]. The real part of the inelastic scattering form factor was calculated using the double-folding model, the proton and neutron parts of the transition density being calculated using the

23

Tassie Model [59], and the proton and neutron deformation lengths taken from Ref. [40]. The imaginary part of the inelastic form factor was obtained by deforming the Woods-Saxon imaginary potential using the isoscalar deformation length of Ref. [40]. Following the conclusions of Ref. [40], we adopted the simplifying assumption of a pure $(1p_{3/2})^2$, S-wave $(J = L = 0)$ configuration for the two neutrons in the ^{6}He ground state, where J is the internal angular momentum of the $2n$ cluster and L its orbital angular momentum with respect to the ^{4}He core. The $\langle ^6\text{He}|^4\text{He} + 2n\rangle$ overlaps were calculated using the Bayman-Kallio method [60] and the spectroscopic amplitude was adjusted to give the best description of the data. Also following the conclusions of Ref. [40], the two-step sequential (^{6}He, ^{5}He; ^{5}He, ^{4}He) and indirect (^{6}He, $^6\text{He}^*_{2+}$; $^6\text{He}^*_{2+}$, ^{4}He) transfer paths were omitted as having negligible influence at the incident energies concerned. Test calculations for the $E_{\text{c.m.}} = 5.82$ MeV data supported this conclusion. Values of N_{R}, $W(r)$, r_W, a_W and the spectroscopic amplitude for the $\langle ^6\text{He}|^4\text{He} + 2n\rangle$ overlap $\text{SA}_{\text{g.s.}}$ are given in Table I. The best-fit value of $\text{SA}_{\text{g.s.}}$ is somewhat smaller than the expected value of about 1.25 quoted in Khoa and von Oertzen [40], but is close to 0.85, the smallest empirical value they obtained.

The calculated differential cross sections of elastic scattering are compared to the experimental data in Fig. 8. To display the variation of the angular distribution as a function of energy, the CRC calculations for the previous energy bins are shown together by the dashed lines. Except for the last energy bin at 2.7 MeV, the calculated cross sections reproduce the data. The calculated cross sections vary smoothly as a function of $E_{\text{c.m.}}$, while the reaction parameters are nearly constant. At 2.7 MeV, the cross sections are suddenly enhanced and the radius and diffuseness parameters of the imaginary potential drastically change. This result indicates that elastic scattering predominantly proceeds via direct reactions outside of the region near $E_{\text{c.m.}} = 2.7$ MeV. It supports the conjecture made from the excitation functions that there is no sizable resonance in the region from 9.4 to 13.4 MeV in E_{x} of ^{10}Be except for the 4^+ state at 10.15 MeV.

The resonance of another 4^+ state at 11.76 MeV, therefore, was not identified at the corresponding energy of $E_{\text{c.m.}} = 4.4$ MeV. The upper limit of the partial decay width was estimated by searching the limit where the resonance can be identified as a peak over the contribution of non-resonant scattering in the spectrum. The resulting value is $\Gamma_\alpha/\Gamma < 0.15$, or $\Gamma_\alpha < 20$ keV for the known Γ value of 121(10) keV [51].

The differential cross sections of inelastic ^{6}He + α scattering to the ^{6}He 2^+ state are

24

shown in Fig. 9 together with the CRC calculations denoted by the solid lines. The CRC calculations for the magnitude of the cross sections are in good agreement with the experimental data, suggesting the validity of the framework of reaction analysis and the adopted optical-model potential parameters. The diffractive pattern is slightly out of phase with respect to the CRC predictions in the energy bin of $E_{\text{c.m.}} = 4.2$ MeV, where a resonance is inferred from the excitation function spectra. The experimental angular distribution peaks at 90° and symmetrically decreases towards 60° and 120°. This is characteristic of an angular momentum of $L = 2$.

B. Two-neutron emission channel

The angle-integrated excitation function was deduced for the $^6\text{He}(\alpha, 2n)^8\text{Be}$ channel. The reaction vertex was converted to reaction energy E_{reac} after correcting for the energy loss using a program based on the SRIM code [47]. The cross section of the reaction as a function of center-of-mass energy $E_{\text{c.m.}}$ is shown in Fig. 10. Note that above 3 MeV, the spectrum includes also the contribution from the ^8Be 2^+ state. The contribution of the ground state, however, more likely dominates as the z_{reac}-Q_{total} data (Fig. 6(a)) agree well with the simulation for the ground state (Fig. 6(b)). These two components would be differentiated by analyzing the correlations between two α particles that were not measured in this study. The vertical error bars are statistical only, while the horizontal error bars denote the sum of statistical and systematic errors. The latter comes from the ambiguity in locating the reaction vertex which is estimated to be ± 10 mm. The cross section increases from the reaction threshold of the $^6\text{He}(\alpha, 2n)^8\text{Be}$ reaction at 1.06 MeV toward higher energies. It is clear that no significant resonance strength exists in the energy region covered in the present study. There is a minor peak structure at 2.5 MeV. It is difficult to judge whether this is due to a resonance or to a statistical fluctuation, particularly without the corresponding information from an angular distribution. In the former case, it would be possible that it originates from the 10.15-MeV 4^+ state with nearly the same resonance energy. A fit with a Voigt function [50] was made to estimate the possible partial width $\Gamma_{^8\text{Be}}$. Three different backgrounds, namely linear, quadratic, and exponential functions, were tested. The resonance energy was set to the result from the elastic channel (2.56 MeV) and varied within the error (0.15 MeV), while the experimental resolution was fixed to 0.25 MeV

25

rms, which arises from the uncertainty in reaction energy (0.1 MeV) and that in vertex determination (0.2 MeV). The resulting $\Gamma_{^8\text{Be}}/\Gamma$ value is 0.09(5) and this gives an upper limit of $\Gamma_{^8\text{Be}}/\Gamma \sim 0.15$ for this possible decay branch.
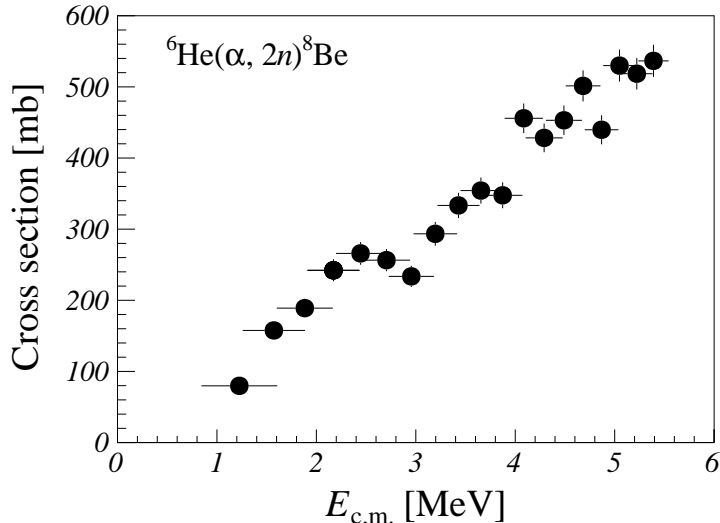

FIG. 10. Angle-integrated excitation function for the $^6\text{He}(\alpha, 2n)^8\text{Be}$ channel.

V. DISCUSSION

The present study identified a 4^+ state with a large α decay width $\Gamma_\alpha/\Gamma = 0.49(5)$ at 9.98(15) MeV in ^{10}Be. The observed state most likely corresponds to the known 4^+ level at 10.15(2) MeV [31, 32] given the observed excitation energy and spin-parity. In previous studies [24, 32, 33], this state is considered the 4^+ member of a rotational band built on the second 0^+ state at 6.1793(7) MeV [51]. The excitation energies of ^{10}Be states are plotted against $J(J+1)$ in Fig. 11. The linear extrapolation from the 0_2^+ state and the 2^+ state at 9.560(20) MeV [51] indeed nicely agrees with the 10.15-MeV state in energy. The large moment of inertia from the narrow level spacing of the band members is well explained by the σ-type molecular orbital structure from both cluster-model calculations [21, 22, 25] and microscopic calculations based on the antisymmetric molecular dynamics (AMD) method [15, 24, 26]. In this picture, the valence neutrons are delocalized over the two clusterized α cores and the extension along the α cores' axis gives strong deformative characteristics to ^{10}Be. The large decay width for α emission indicates a high degree of clusterization in this
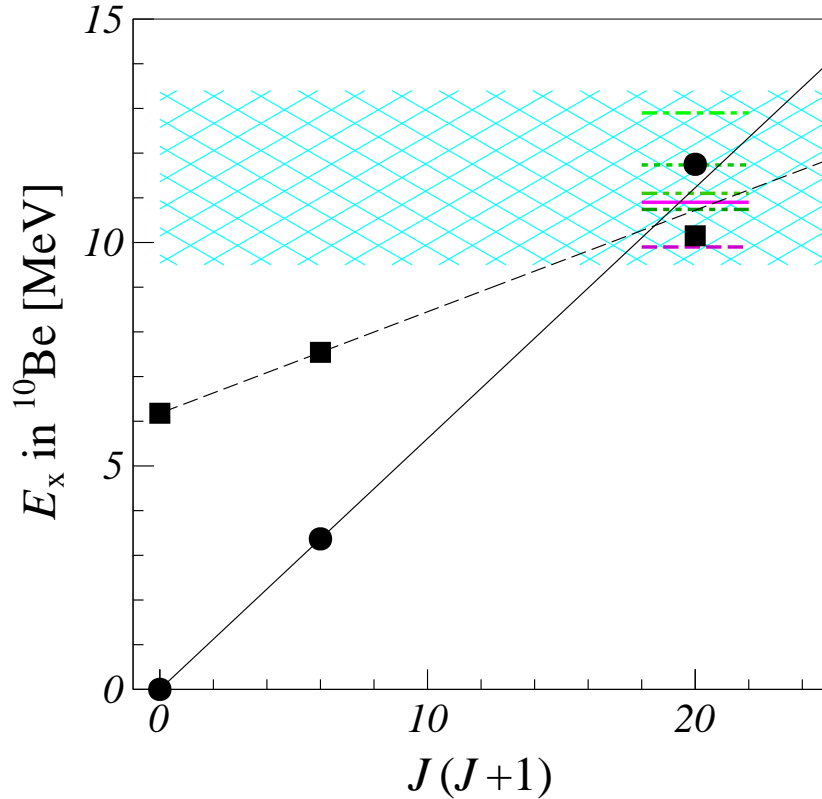
26

FIG. 11. (Color online) Plot of E_{x} $vs.$ $J(J+1)$ for ^{10}Be. The band members of the ground and the second 0^+ states are shown by the circles and squares, respectively. The linear extrapolation using the 0^+ and 2^+ states is shown for each band. The horizontal lines at $J = 4$ denote predicted level energies of the 4^+ member of the ground state band from the β-γ constraint AMD method [24] (solid line), the variational AMD method [15] (dashed line), the four-body cluster model [21] (dotted line), the molecular orbital model [16] (dot-dashed line), the semi-microscopic algebraic cluster model [18], (double-dot-dashed line), and the multi-cluster generator coordinate method [19], (triple-dot-dashed line). The data of Refs.[16, 21] were obtained from the calculated values with respect to the threshold energy of $2\alpha + 2n$ at 8.386 MeV. The shaded area denotes the energy domain covered by the present study.

556 4^+ state and supports this type of cluster structure. An α spectroscopic factor of 3.1(2) is
557 estimated in a recent analysis of the measured partial width [61]. This value is as large
558 as the spectroscopic factors of about 1.5 for the ground-state band members of ^{8}Be with
559 well-developed two α clusters [61, 62].

In addition to the 0_2^+ state, theoretical studies [15, 16, 22, 24] predict a π-type cluster structure for the 0^+ ground state, in which valence neutrons are extending perpendicular to the axis of the two α cores. Given the 2^+ state at 3.37 MeV, the 4^+ state of the $0_{\text{g.s.}}^+$ band is anticipated at around 11 MeV as seen in the linear extrapolation shown in Fig. 11. In previous studies [24, 33], the 4^+ state at 11.76(2) MeV is considered the most likely candidate for the 4^+ member of the $0_{\text{g.s.}}^+$ band because of its excitation energy and spin-parity. In the present study, however, there was no resonance observed around $E_{\text{x}} = 11.8$ MeV ($E_{\text{c.m.}} = 4.4$ MeV). This is in stark contrast with the significant resonance strength of the 4^+ state of the 0_2^+ band at 10.2 MeV. The α decay width of the 11.8-MeV state is estimated less than 20 keV and is much smaller than $\Gamma_\alpha = 145(15)$ keV deduced for the 10.2-MeV state. Such a difference is unexpected as both 4^+ states belong to the rotational bands of the clusterized 0^+ states. Nearly the same spectroscopic amplitudes of $^6\text{He} + \alpha$ are predicted for these 4^+ states in the microscopic $2\alpha + 2n$ four-cluster-model [21]. The present result does not agree with this prediction. The small spectroscopic amplitude of the 4^+ member is also unlike the ground state 0^+ band of ^8Be, despite what appears to be a similar moment of inertia. The α spectroscopic factors are predicted to be equally large in all 0^+, 2^+, and 4^+ states in ^8Be [62], which is supported by the folding potential model that well describes the level energies and widths of these states [63].

There are two possible scenarios to account for the hindered strength of the 4^+ member of the $0_{\text{g.s.}}^+$ band. First is the possibility that the 4^+ state at 11.8 MeV does not belong to the $0_{\text{g.s.}}^+$ band, and the real band member exists outside the energy window of the present study ($E_{\text{c.m.}} = 2-6$ MeV or $E_{\text{x}} = 9.4-13.4$ MeV). This scenario implies an unusual level spacing for the ground state band. On the contrary, regardless of the framework, most theoretical studies [15, 16, 18, 19, 21, 24] predict the 4^+ state of the $0_{\text{g.s.}}^+$ band in the energy range $E_{\text{x}} = 10-13$ MeV (Fig. 11), the region anticipated from the proportionality to $J(J+1)$. The second scenario is that the 4^+ state does belong to the $0_{\text{g.s.}}^+$ band, but with a reduced degree of clusterization that hinders the decay branch for α emission. The weakening of clustering in the 4^+ state is pointed out by an early AMD study of ^{10}Be [15]. In this prediction, the 0^+ ground state of ^{10}Be is highly clusterized, as confirmed in another later AMD study [64]. However, the component of two-α cores in the rotational band members is gradually reduced as the total spin increases. The origin of the dissociation of α clusters is attributed to the nuclear spin-orbit force. A stronger spin-orbit force yields a smaller

amplitude of two α cores in the 2^+ and 4^+ states of the $0^+_{\text{g.s.}}$ band. This scenario naturally explains why the four cluster model of $2\alpha + 2n$ overpredicts the spectroscopic amplitude of ^{6}He $+ \alpha$. In the molecular model, α clusters are assumed as the basis of wave functions, and thus the model does not incorporate the effects of their dissociation. On the other hand, the AMD method adopts Slater determinants where the spatial part of each single-particle wave function is a Gaussian function, and does not require the assumption of inert cluster cores [65]. This allows one to study the formation and dissociation of α clusters within one framework. The absence of resonance strength of the 4^+ state at 11.8 MeV agrees more with the interpretation of AMD calculations, which predict the limits of α clustering in higher spin members of the $0^+_{\text{g.s.}}$ band due to the spin-orbit force.

It is known that the spin-orbit force dissociates α clusters in high-spin states of ^{20}Ne [66–68] or ^{44}Ti [67]. Such an effect is considered to be hindered in ^{8}Be as it is a lighter nucleus with a weaker spin-orbit force [67]. On the other hand, recent AMD studies on ^{12}C [64, 69], an isotone of ^{10}Be, point out that the effect of the spin-orbit force is pronounced by the sub-shell closure at $N = 6$ and this explains the small degree of clusterization for its ground state. In ^{10}Be, this effect might be more important for the $0^+_{\text{g.s.}}$ band, which primarily consists of p-shell configurations [15], than for the intruder 0^+_2 band. The present result for ^{10}Be implies a delicate competition between the persistence of the clusters in ^{8}Be and their dissociation by the spin-orbit force as the number of neutrons increases toward the neutron drip line.

Finally, we discuss the present results in comparison with theoretical calculations of resonant α scattering of ^{6}He in the framework of the four-body cluster model [14, 23]. The study using the resonating-group method predicts drastic changes in the scattering phase shift of $L = 3$ at $E_{\text{c.m.}} = 3.7$ MeV and $L = 0$ around 4.5 MeV for elastic scattering [14]. The angular distribution at 3.7 MeV is predicted to show enhanced cross sections with an oscillation characteristic of $L = 3$. However, in the present measurement, sizable resonances are clearly absent in the corresponding energy region in the elastic channel. Inelastic scattering to the ^{6}He 2^+ state was studied in a more recent work based on the generalized two-center cluster approach, where the reaction of ^{6}He $+ \alpha$ and the structure of ^{10}Be are described in a unified manner [23]. Excitation functions for $L = 1, 2$ were calculated and a few resonances are proposed in the energy region of $E_{\text{c.m.}} = 2-7$ MeV. The possible resonance of $L = 2$ inferred at 4.4 MeV in the present study is in line with the $L = 2$ resonance predicted at

624 4 MeV. It originates from a 0^+ state in ^{10}Be with a large amplitude of the $\alpha + {}^6$He(2^+) com-

625 ponent, thus having a sizable strength in the inelastic channel. Further theoretical studies,

626 particularly on excitation functions for the elastic channel that are not presented in Ref. [23],

627 might be useful to interpret the inferred resonance.

628 **VI. CONCLUSION**

629 Scattering of neutron-rich ^{6}He nuclei on α particles was studied at the *TwinSol* facil-

630 ity [42] at the University of Notre Dame. A time projection chamber, PAT-TPC [43], using

631 He:CO_2 90:10 gas at atmospheric pressure was operated in the active-target mode to pro-

632 vide a gaseous ^{4}He target and track the beam and reaction products traversing the target.

633 This unique capability significantly lowered the threshold for the energy of helium nuclei,

634 allowing a continuous measurement of the excitation functions over a wide energy range

635 with the unambiguous reconstruction of angular distributions, which are difficult to obtain

636 in conventional studies using non-active targets.

637 Excitation functions and angular distributions were thus measured for elastic scattering

638 and inelastic scattering to the ^{6}He 2^+ state below a center-of-mass energy of 6 MeV. The

639 present system also allowed us to measure the excitation function of the ^{6}He(α, $2n$)^{8}Be

640 channel, which requires the detection of low-energy α particles following the decay of un-

641 bound ^{8}Be. The resulting excitation function of elastic scattering shows a resonance at

642 $E_{\text{c.m.}} = 2.56(15)$ MeV, or an excitation energy $E_{\text{x}} = 9.98(15)$ MeV in ^{10}Be. A spin-parity

643 of 4^+ was assigned from the angular distribution. The partial α decay width was estimated

644 to be $\Gamma_\alpha/\Gamma = 0.49(5)$. These results obtained from the unambiguously-identified recoiling

645 α particles confirm the previous results obtained for the state at 10.15(2) MeV without

646 differentiating the ^{6}He and α particles, but with considerably better statistics [32]. The

647 assignment of 4^+ supports the claim of Ref. [32] that the 10.15-MeV state corresponds to a

648 member of the 0_2^+ band.

649 The large partial width for α decay indicates a highly-developed α cluster structure in this

650 4^+ state. It is consistent with most theoretical predictions proposing the σ-type molecular

651 orbital structure for the 0_2^+ band. On the contrary, no resonance strength for another 4^+

652 state was observed in this energy region, where the 4^+ member of the ground state 0^+ band

653 is expected. Except for the region near $E_{\text{c.m.}} = 2.6$ MeV, the angular distributions vary

30

smoothly as a function of energy, which is well reproduced by coupled-reaction channels calculations. The hindered resonance strength is incompatible with theoretical calculations done in the framework of the four-body cluster model, which predict a sizable spectroscopic amplitude of ^{6}He $+ \alpha$ due to a π-type molecular orbital structure [21]. However, it is in line with the results from an AMD study where the α clusters of the 0^+ ground state are gradually dissociated by the nuclear spin-obit force as the spin increases to its 2^+ and 4^+ rotational band members [15]. The present results support the limits of clustering in ^{10}Be due to the spin degree-of-freedom, and calls for more detailed spectroscopy of individual cluster states in ^{10}Be and related microscopic theoretical studies.

The excitation function of the inelastic channel shows a slight enhancement at $E_{\text{c.m.}} = 4.4$ MeV that may be due to a resonance. An angular momentum of $L = 2$ is suggested from the angular distribution. This resonance may be related to a 0^+ state with a large ^{6}He$(2^+) + \alpha$ component, which is predicted around 4 MeV [23].

The angle-integrated excitation function was obtained for the ^{6}He$(\alpha, 2n)^8$Be channel, with no strong resonance observed in the region of $E_{\text{c.m.}} = 1-5$ MeV. While the cross section is slightly enhanced around $E_{\text{c.m.}} = 2.5$ MeV, it is uncertain whether this is a statistical fluctuation or a possible resonance originating from the 4^+ state at 10.15 MeV. As measured in this study, this 4^+ state has a large partial decay width of $\Gamma_\alpha/\Gamma = 0.49(5)$ to the ^{6}He$(0^+) + \alpha$ final state, which is considered to be an indication of α clustering. The result of the ^{6}He$(\alpha, 2n)^8$Be channel, in contrast, gives an upper limit of $\Gamma_{^8\text{Be}}/\Gamma \sim 0.15$ for the decay to ^{8}Be, a nucleus with a pronounced 2α structure. It will be interesting to see if the partial width to such a three body system (^{8}Be $+ 2n$) is sensitive to various α-cluster structures predicted for ^{10}Be.

VII.   ACKNOWLEDGEMENT

31

686 [1] J.A. Wheeler, Phys. Rev. **52**, 1083 (1937).

687 [2] D.M. Dennison, Phys. Rev. **96**, 378 (1954).

688 [3] H. Morinaga, Phys. Rev. **101**, 254 (1956).

689 [4] F. Hoyle, Astrophys. J. Suppl. Ser. **1**, 121 (1954).

690 [5] C.W. Cook, W.A. Fowler, C.C. Lauritsen, and T. Lauritsen, Phys. Rev. **107**, 508 (1957).

691 [6] T. Wakasa *et al.*, Phys. Lett. B **653**, 173 (2007).

692 [7] A.H. Wuosmaa, R.R. Betts, B.B. Back, M.Freer, B.G. Glagola, Th. Happ, D.J. Henderson, P.
693 Wilt, and I.G. Bearden, Phys. Rev. Lett. **68**, 1295 (1992).

694 [8] A. Tohsaki, H. Horiuchi, P. Schuck, and G. Röpke, Phys. Rev. Lett. **87**, 192501 (2001).

695 [9] Y. Funaki, T. Yamada, H. Horiuchi, G. Röpke, P. Schuck, and A. Tohsaki, Phys. Rev. Lett.
696 **101**, 082502 (2008).

697 [10] T. Kawabata *et al.*, Phys. Lett. B **646**, 6 (2007).

698 [11] M. Seya, M. Kohno, and S. Nagata, Prog. Thor. Phys. **65**, 204 (1981).

699 [12] Y. Kanada-En'yo, H. Horiuchi, and A. Ono, Phys. Rev. C **52**, 628 (1995).

700 [13] W. von Oertzen, Z. Phys. A **354**, 37 (1996).

701 [14] K. Fujimura, D. Baye, P. Descouvemont, Y. Suzuki, and K. Varga, Phys. Rev. C **59**, 817
702 (1999).

703 [15] Y. Kanada-En'yo, H. Horiuchi, and A. Dote, Phys. Rev. C **60**, 064304 (1999).

704 [16] N. Itagaki and S. Okabe, Phys. Rev. C **61**, 044306 (2000).

705 [17] Y. Ogawa, K. Arai, Y. Suzuki, and K. Varga, Nucl. Phys. A **673**, 122 (2000).

706 [18] L. Hernández de la Peña, P.O. Hess, G. Lévai, and A. Algora, J. Phys. G **27**, 2019 (2001).

707 [19] P. Descouvemont, Nucl. Phys. A **699**, 463 (2002).

708 [20] N. Itagaki, S. Hirose, T. Otsuka, S. Okabe, and K. Ikeda, Phys. Rev. C **65**, 044302 (2002).

709 [21] K. Arai, Phys. Rev. C **69**, 014309 (2004).

710 [22] M. Ito, K. Kato, and K. Ikeda, Phys. Lett. B **588**, 43 (2004).

711 [23] M. Ito, Phys. Lett. B **636**, 293 (2006).

712 [24] T. Suhara and Y. Kanada-En'yo, Prog. Theo. Phys. **123**, 303 (2010).

[25] N. Itagaki, S. Okabe, and K. Ikeda, Phys. Rev. C **62**, 034301 (2000).

[26] Y. Kanada-En'yo and H. Horiuchi, Phys. Rev. C **68**, 014319 (2003).

[27] D. Suzuki *et al.*, Phys. Rev. Lett. **103**, 152503 (2009).

[28] D. Suzuki, Eur. Phys. J A **48**, 130 (2012).

[29] N. Soić *el al.* Europhys. Lett. **34**, 7 (1996).

[30] N. Curtis, D.D. Caussyn, N.R. Fletcher, F. Maréchal, N. Fay, and D. Robson, Phys. Rev. C **64**, 044604 (2001).

[31] M. Milin *et al.*, Nucl. Phys. A **753**, 263 (2005).

[32] M. Freer *et al.*, Phys. Rev. Lett. **96**, 042501 (2006).

[33] H.G. Bohlen, T. Dorsch, Tz. Kokalova, W. von Oertzen, Ch. Schulz, and C. Wheldon, Phys. Rev. C **75**, 054604 (2007).

[34] S. Ahmed *et al.*, Phys. Rev. C **69**, 024303 (2004).

[35] H. Yamaguchi *et al.*, Phys. Rev. C **83**, 034306 (2011).

[36] G.M. Ter-Akopian *et al.*, Phys. Lett. B **426**, 251 (1998).

[37] R. Raabe *et al.*, Phys. Lett. B **458**, 1 (1999).

[38] R. Raabe *et al.*, Phys. Rev. C **67**, 044602 (2003).

[39] K. Rusek and K.W. Kemper, Phys. Rev. C **61**, 034608 (2000).

[40] D.T. Khoa and W. von Oertzen, Phys. Lett. B **595**, 193 (2004).

[41] K.P. Artemov, M.S. Golovkov, V.Z. Goldberg, V.V. Pankratov, A.E. Pakhomov, I.N. Serikov, and V.A. Timofeev, Sov. J. Nucl. Phys. **55**, 1460 (1992).

[42] F. Becchetti, M.Y. Lee, T.W. O'Donnell, D.A. Roberts, J.J. Kolata, L.O. Lamm, G. Rogachev, V. Guimarães, P.A. DeYoung, and S. Vincent, Nucl. Instr. and Meth. Phys. Res., Sect. A **505**, 377 (2003).

[43] D. Suzuki *et al.*, Nucl. Instr. and Meth. Phys. Res., Sect. A **691**, 39 (2012).

[44] Y. Giomataris, Ph. Rebourgeard, J.P. Robert, and G. Charpak, Nucl. Instr. and Meth. Phys. Res., Sect. A **376**, 29 (1996).

[45] P. Baron, D. Calvet, E. Delagnes, X. de la Broise, A. Delbart, F. Druillole, E. Mazzucato, E. Monmarthe, F. Pierre, and M. Zito, IEEE Transactions on Nuclear Science NS-55, 1744 (2008).

[46] Y. Kudenko, Representing the T2K Collaboration, Nucl. Instr. and Meth. Phys. Res., Sect. A **598**, 289 (2009).

[47] J.F. Ziegler, M.D. Ziegler, and J.P. Biersack., Nucl. Instr. and Meth. Phys. Res., Sect. B **268**, 1818 (2010).

[48] G. Audi, A.H. Wapstra, C. Thibault, Nucl. Phys. A **729**, 337 (2003).

[49] D.R. Tilley, C.M. Cheves, J.L. Godwin, G.M. Hale, H.M. Hofmann, J.H. Kelley, C.G. Sheu, and H.R. Weller, Nucl., Phys. A **708**, 3 (2002).

[50] W. Voigt, Münch. Ber., 603 (1912).

[51] D.R. Tilley, J.H. Kelley, J.L. Godwin, D.J. Milener, J.E. Purcell, C.G. Sheu, and H.R. Weller, Nucl., Phys. A **745**, 155 (2004).

[52] A.M. Lane and R.G. Thomas, Phys. Mod. Phys. **30**, 257 (1958).

[53] I.J Thompson, Comput. Phys. Rep. **7**, 167 (1988).

[54] J. Cook, Comput. Phys. Commun. **25**, 125 (1982).

[55] G. Bertsch, J. Borysowicz, H. McManus, and W.G. Love, Nucl. Phys. A **284**, 399 (1977).

[56] J.S. McCarthy, I. Sick, and R.R. Whitney, Phys. Rev. C **15**, 1396 (1977).

[57] G.R. Satchler and W.G. Love, Phys. Rep. **55**, 183 (1979).

[58] J.S. Al-Khalili, J.A. Tostevin, and I.J. Thompson, Phys. Rev. C **54**, 1843 (1996).

[59] L.J. Tassie, Australian J. Phys. **9**, 407 (1956).

[60] B.F. Bayman and A. Kallio, Phys. Rev. **156**, 1121 (1967).

[61] H.T. Fortune and R. Sherr, Phys. Rev. C **84**, 024304 (2011).

[62] D. Kurath, Phys. Rev. C **7**, 1390 (1973).

[63] P. Mohr, H. Abele, V. Kölle, G. Staudt, H. Oberhummer, and H. Krauss, Z. Phys. A **349**, 339 (1994).

[64] N. Itagaki, S. Aoyama, S. Okabe, and K. Ikeda, Phys. Rev. C **70**, 054307 (2004).

[65] Y. Kanada-En'yo, Phys. Rev. Lett. **81**, 5291 (1998).

[66] T. Tomoda and A. Arima, Nucl. Phys. A **303**, 217 (1978).

[67] T. Yamada, Phys. Rev. C **42**, 1432 (1990).

[68] M. Kimura, Phys. Rev. C **69**, 044319 (2004).

[69] Y. Kanada-En'yo, Prog. Theo. Phys. **117**, 655 (2007).

34